

Single-Step Fabrication of High-Performance Extraordinary Transmission Plasmonic Metasurfaces Employing Ultrafast Lasers

Carlota Ruiz de Galarreta,^{*,§} Noemi Casquero,[§] Euan Humphreys, Jacopo Bertolotti, Javier Solis, C. David Wright, and Jan Siegel^{*}



Cite This: *ACS Appl. Mater. Interfaces* 2022, 14, 3446–3454



Read Online

ACCESS |



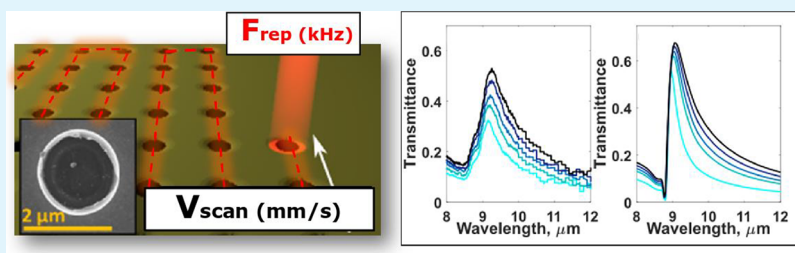
Metrics & More



Article Recommendations



Supporting Information



ABSTRACT: Plasmonic metasurfaces based on the extraordinary optical transmission (EOT) effect can be designed to efficiently transmit specific spectral bands from the visible to the far-infrared regimes, offering numerous applications in important technological fields such as compact multispectral imaging, biological and chemical sensing, or color displays. However, due to their subwavelength nature, EOT metasurfaces are nowadays fabricated with nano- and micro-lithographic techniques, requiring many processing steps and carrying out in expensive cleanroom environments. In this work, we propose and experimentally demonstrate a novel, single-step process for the rapid fabrication of high-performance mid- and long-wave infrared EOT metasurfaces employing ultrafast direct laser writing. Microhole arrays composing extraordinary transmission metasurfaces were fabricated over an area of 4 mm² in timescales of units of minutes, employing single pulse ablation of 40 nm thick Au films on dielectric substrates mounted on a high-precision motorized stage. We show how by carefully characterizing the influence of only three key experimental parameters on the processed micro-morphologies (namely, laser pulse energy, scan velocity, and beam shaping slit), we can have on-demand control of the optical characteristics of the extraordinary transmission effect in terms of transmission wavelength, quality factor, and polarization sensitivity of the resonances. To illustrate this concept, a set of EOT metasurfaces having different performances and operating in different spectral regimes has been successfully designed, fabricated, and tested. Comparison between transmittance measurements and numerical simulations has revealed that all the fabricated devices behave as expected, thus demonstrating the high performance, flexibility, and reliability of the proposed fabrication method. We believe that our findings provide the pillars for mass production of EOT metasurfaces with on-demand optical properties and create new research trends toward single-step laser fabrication of metasurfaces with alternative geometries and/or functionalities.

KEYWORDS: ultrafast laser processing, metasurfaces, extraordinary transmission, plasmonics, micro-fabrication

1. INTRODUCTION

Due to a progressive miniaturization of technologies such as mobile phone cameras, optical circuits, or sensing, optical metasurfaces are becoming one of the most promising key components toward the development of next generation lightweight devices. Metasurfaces consist of two-dimensional, subwavelength (typically resonant) building blocks, which can be either periodically or randomly arranged, and can be engineered to provide on-demand light control.^{1–8} Contrary to conventional bulky optics, the ability to tailor light offered by metasurfaces does not rely on propagation effects (such as optical path length differences or linear absorption) but instead comes from abrupt amplitude and phase local or global discontinuities induced by localized and/or coupled resonances.^{1,2} As a result, arrays of resonators can be specifically

engineered to mimic and even to outperform the functionalities of classical optics in a lightweight fashion.^{1–5,8} Among the range of available metasurface functionalities, plasmonic-based metasurfaces exploiting the extraordinary optical transmission (EOT) effect have attracted much attention over the last years, as such devices are expected to play an important role in compact biological and chemical sensing,^{9–11} structural color generation, or multispectral imaging.^{3,12,13} The EOT

Received: October 15, 2021

Accepted: December 17, 2021

Published: January 4, 2022



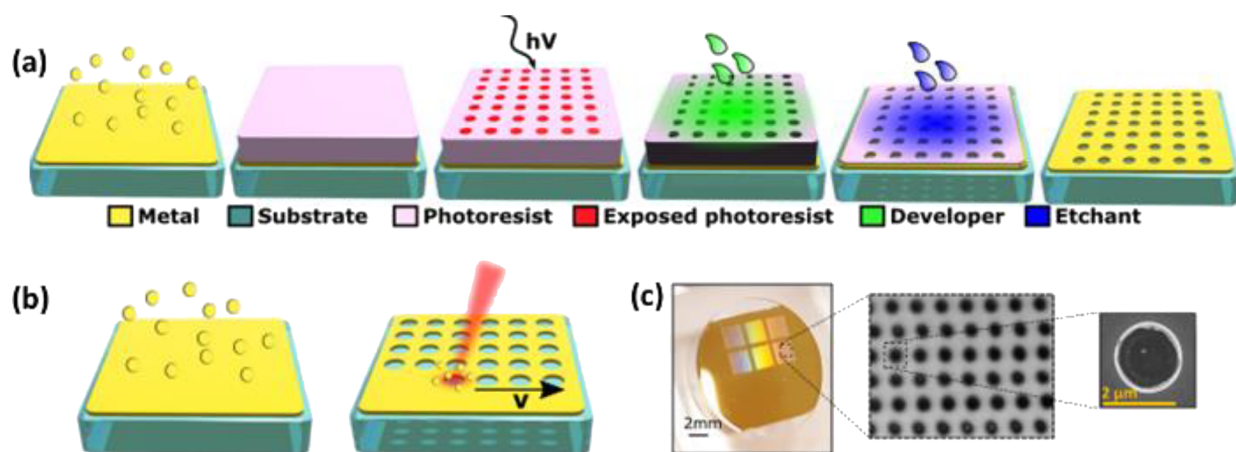


Figure 1. (a) Schematics of a typical lithographic process for micro- and nano-patterning of the EOT metasurfaces, consisting of various fabrication steps. From left to right: after depositing a thin metal film, a photoresist layer is spin-coated on the top of the surface and exposed to electron or photolithography to modify the solubility of the exposed regions. Such regions are then removed employing a developer, followed by a wet/dry etching process to eliminate the material from the exposed regions. The process ends by removing the photoresist/chemical leftovers, typically in acetone. (b) Alternative fabrication routine proposed in this work, consisting of direct laser patterning employing ultrafast scanned lasers. (c) Macroscopic view of one of the processed samples, with six 4 mm² areas patterned on it. The insets show an optical microscope and scanning electron microscopy (SEM) image, confirming the micrometric geometrical features.

phenomenon consists of a specific frequency band being transmitted through a periodically arranged array of sub-wavelength nanoholes in an optically thin film. In particular, high transmission peaks appear close to the first Wood anomaly, i.e., at the frontier between the diffractive and sub-diffractive optical regimes.^{13–15} The occurrence of this phenomenon has been studied in detail over the last years and has been attributed to a resonant interaction between holes arranged in a lattice, assisted by highly confined fields associated to surface waves such as plasmon¹⁵ or phonon polaritons.^{14,15} The amount of transmission, the bandwidth, and spectral position of the EOT effect can be therefore controlled by design via simply tuning the geometrical parameters (namely, hole size, shape, and periodicity) and/or constituent materials of the film, substrate, and/or cover layer.^{8–10}

While EOT metasurfaces introduce indubitable benefits to current optical and photonic technologies, their reliable large scale fabrication is currently at a low stage of maturity in terms of throughput and cost. This is primarily due to the small size of the patterned features and the high resolution required for the successful realization of metasurfaces (ranging from tens of nanometers to units of microns for electromagnetic metasurfaces operating from the ultraviolet to the mid-infrared spectral region, respectively).^{1–3} Their fabrication is currently achieved via established nanostructuring processes, on which an excellent overview can be found elsewhere.¹⁶ As generically depicted in Figure 1a, among them, mask-based techniques such as electron-beam lithography or photolithography combined with lift-off, nanoimprint, or wet/dry etching are nowadays the predominant fabrication methods chosen. Such techniques can indeed provide a precise spatial resolution down to tens of nanometers^{17–19} but at the same time require for expensive equipment to be operated under cleanroom environments.^{17–19} An alternative technique with an extraordinarily high degree of versatility and throughput is based on ultrafast laser processing (ULP). This technique is arguably one of the most promising routes toward clean, large-scale, and mass-production of nano- and micro-patterned devices, as it is

based on single-step patterning procedures that do not require the use of polymer masks and contaminants nor cleanroom equipment.^{16,20} Employing sub-picosecond laser pulses, one can reduce the pulse energy required to trigger ablation while achieving sharp contours in a wide variety of soft and brittle materials.^{20,21} To date, a wide range of nano- and micro-features have been successfully fabricated using ultrafast lasers, including ripples and grooves, spikes, arrays of holes or pillars, hierarchical shapes or compositional and random structures.²⁰ Nevertheless, while ULP techniques have been now extensively explored toward the realization of, e.g., high density data storage,²² biomimetic structures,²⁰ photonic and microfluidic devices in transparent materials,²³ or functionalized surfaces for wettability control,^{24,25} their potential toward fabrication of metasurfaces remains highly underexplored. Examples of recent works on ULP aiming at the production of metasurfaces include the fabrication of the arrays of Si Mie resonators via direct interference laser patterning,²⁶ arrays of Si nanoparticles via laser-induced forward transfer,²⁷ and arrays of microbumps in Au films using direct laser writing (DLW).²⁸ Additional work about randomly structured metasurfaces for structural color generation and color encryption employing ultrafast lasers has been also recently reported.^{29,30}

In this paper, we introduce a novel fabrication process for the rapid realization of EOT metasurfaces in a single step based on DLW and thus free from expensive cleanroom environments. As depicted in Figure 1b,c, this is achieved by focusing a pulsed laser at the surface of a thin metallic film deposited on a dielectric substrate, which is mounted on a motorized stage that moves in a zigzag fashion. By selecting the (previously calibrated) experimental setup parameters, a set of EOT devices with different optical and morphological characteristics has been designed, successfully fabricated over an area of 4 mm² in units of minutes, and its optical performance tested. Due to its rapid, cost-efficient, and residue free nature, we believe that the herein proposed methodology puts EOT metasurfaces a step closer to industrial, real-world applications.

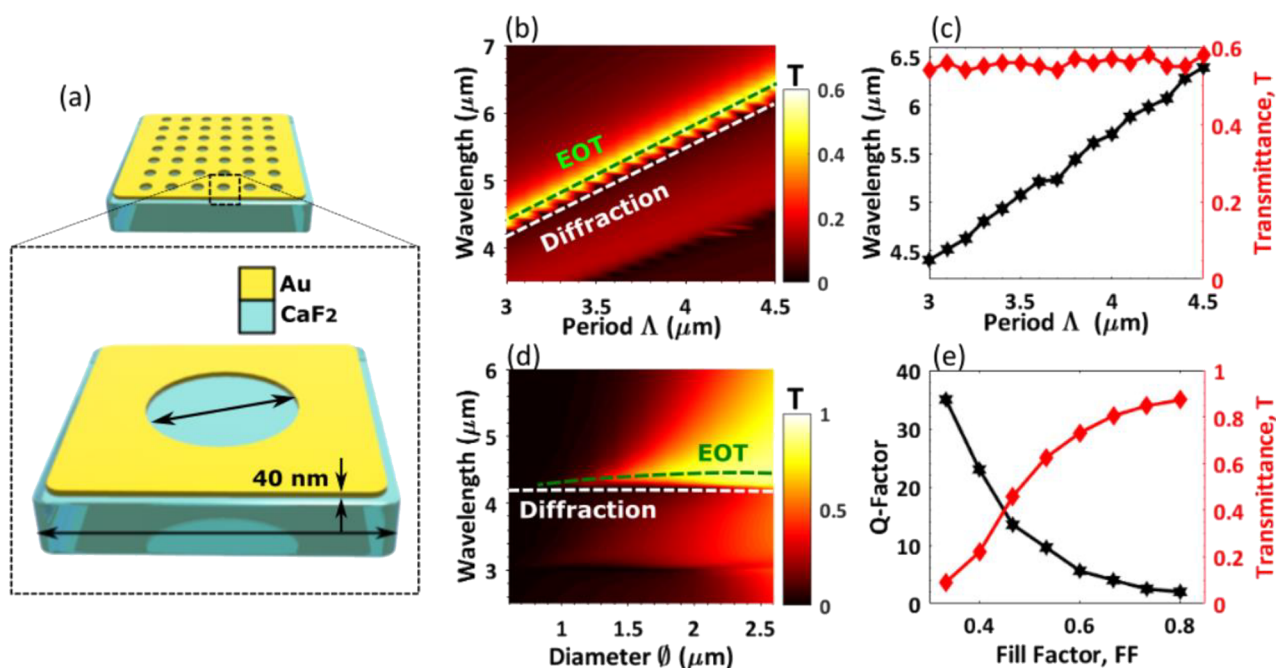


Figure 2. (a) Schematics of the plasmonic EOT metasurface unit cell, showing material distribution, dimensions, and design variables (period Λ and diameter \varnothing). (b) Transmittance spectrum (colorbar) as a function of the period, calculated imposing a constant fill factor of $FF = 0.5$. (c) Details of the variation of the EOT transmission peak wavelength (black) and transmittance (red) as a function of the period. (d) Transmittance spectrum (colorbar) as a function of the hole diameter, calculated while keeping the period at a constant value of $\Lambda = 3 \mu\text{m}$. (e) Details of the variation of the Q -factor (black) and transmittance (red) as a function of the fill factor.

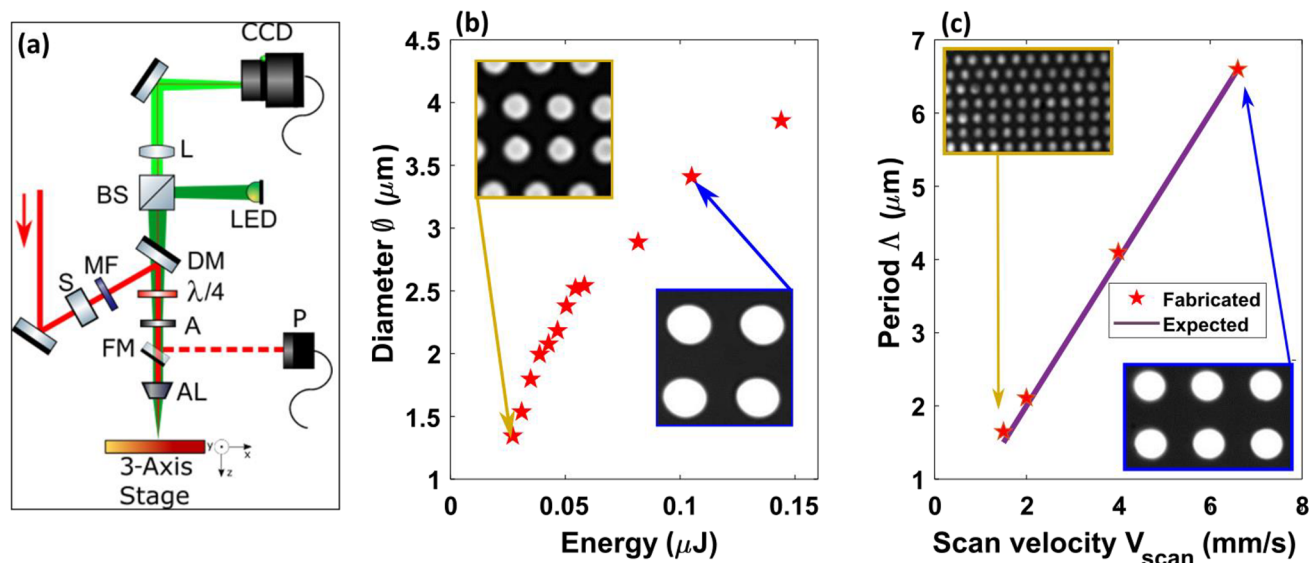


Figure 3. (a) Diagram showing the experimental setup used for the fabrication of EOT metasurfaces employing an ultrafast laser. Red lines correspond to the laser processing beam, whereas the green beam represents the in situ observation path, illuminated by an LED. The labeled components are as follows: slit (S), metallic filter (MF), dichroic mirror (DM), quarter-waveplate ($\lambda/4$), aperture (A), flip mirror (FM), aspheric lens (AL), beam splitter (BS), tube lens (L), and power meter (P). (b) Fabricated hole diameter vs laser pulse energy for NA 0.25. The insets show two representative microscope images of the fabricated holes (field of view is $\sim 12 \mu\text{m} \times 12 \mu\text{m}$). (c) Fabricated hole period vs scanning speed for a repetition rate of $F_{\text{rep}} = 1 \text{ kHz}$. The purple line represents the expected linear trend calculated using eq 3, whereas the red symbols represent the experimentally measured periods fabricated. The insets show representative microscope transmission images of the fabricated hole arrays (field of view is $\sim 18 \mu\text{m} \times 10 \mu\text{m}$).

2. METHODS

2.1. Finite Element Design and Analysis. Prior to the identification and control of the key experimental laser parameters to be employed for the fabrication of the EOT devices, it is necessary to understand the influence of the metasurface geometrical parameters on its optical response. For this purpose, we have carried

out finite element analysis using COMSOL Multiphysics (RF module). The technical details and boundary conditions of the simulation routine are discussed in the [Supplementary Information](#), Section S1.

A generic scheme of the metasurface and its unit cell considered in this work is depicted in [Figure 2a](#). The devices consist of a thin Au film (40 nm) on a CaF_2 dielectric substrate. Au thickness was chosen

to be thick enough to support high quality EOT but thin enough to ensure full single-pulse perforation of the layer (i.e., slightly thicker than the linear optical penetration depth of gold (13 nm), which dominates absorption of ultrafast lasers in high extinction coefficient materials such as metals). CaF₂ was selected as the substrate material due its high transparency across the near, mid-, and long-wave infrared spectral regions.³¹ The film is patterned with identical micro-holes arranged in a square periodic lattice. As shown in Figure 2a, the proposed geometry gives two different geometrical variables, the period Λ and the hole diameter \varnothing . Based on these two degrees of freedom, an additional parameter can be defined, namely, the one-dimensional fill factor FF:

$$FF = \frac{\varnothing}{\Lambda} \quad (1)$$

Figure 2b presents the computed transmittance spectrum of the proposed device as a function of the period while imposing a fixed fill factor of FF = 0.5. As previously reported in literature^{13,15} and confirmed by the results in Figure 2b, the EOT peak appears slightly red-shifted with respect to the frontier between the diffractive and sub-diffractive regimes, that is, when the first diffraction order $\theta_{m \pm 1}$ becomes grazing to the surface, thus giving birth to the first Wood anomaly:

$$\lambda_0 = \Lambda n_{\text{CaF}_2} \quad (2)$$

being λ_0 the free-space excitation wavelength and n_{CaF_2} the refractive index of the substrate³¹ ($n_{\text{CaF}_2} = 1.42$ at a wavelength of $\lambda_0 = 3 \mu\text{m}$ for reference). In Figure 2c, we show fine details of the dependence of both the EOT peak wavelength (black curve) and the amount of transmittance (red curve) with the geometrical period Λ . It can be seen that the EOT peak wavelength is almost linearly proportional to Λ , which is consistent with eq 2. On the other hand, the amount of transmittance remains at a nearly stationary value of $T \sim 0.57$, which is associated to the use of a constant value FF = 0.5, while varying the geometrical period in our simulations.

In Figure 2d, we show the transmittance spectrum as a function of the hole diameter for a fixed geometrical period of $\Lambda = 3 \mu\text{m}$, which implies a variation of the fill factor defined in eq 1. Here, contrary to the previous study, both the diffraction frontier and the EOT peak remain nearly stationary, which is also consistent with eq 2, since Λ is fixed. The details of this simulation are revealed in Figure 2e, where we present the influence of the fill factor on the EOT quality factor (Q -factor = $\lambda_{\text{peak}}/\Delta\lambda$, black curve) and on the amount of transmittance (red curve). As it can be seen from the plot, the quality factor experiences an exponential-like decay when FF increases, accompanied by a logarithmic-like increase in transmittance. This behavior reveals a tradeoff between the bandwidth of the EOT effect and the amount of light transmitted through the array.

2.2. Fabrication Methodology and Calibration of the Processing Parameters. The finite element analysis discussed in the previous section demonstrates that the three main characteristics of the EOT effect (spectral position of the EOT peak, transmittance, and Q -factor) can be controlled by two key geometrical parameters, namely, the period Λ and the hole diameter \varnothing (thus the fill factor FF). Therefore, our fabrication method has been specifically developed and calibrated to provide a flexible control of these geometrical variables. The experimental setup employed for the fabrication of EOT devices is depicted in Figure 3a and is conceptually similar to the optical setups, which have been successfully used for the writing of the embedded optical waveguides described in ref 32. It consists of two optical beam paths, separated by a dichroic mirror:

- Sample processing beam path fed by an ultrafast laser ($\lambda_0 = 1030 \text{ nm}$, $\tau_{\text{pulse}} = 340 \text{ fs}$, maximum repetition rate $F_{\text{rep}} = 2 \text{ MHz}$, Gaussian profile), which is focused at the sample surface using an aspheric lens (AL)
- In situ observation line employing a CCD camera and LED illumination, which is used for alignment purposes and in situ monitoring of the fabrication process

The laser pulse energy is controlled by a combination of a motorized half-waveplate and thin film polarizer (not shown). A 45° flip mirror is placed prior to the aspheric lens to calibrate the incident laser pulse energy with a power meter P. The sample is mounted on a 3-axis stage, with the x-stage being an air-bearing high-speed, high-precision translation stage with scan velocities of up to $V_{\text{scan}} = 20 \text{ mm/s}$. The samples used were 40 nm thick Au films evaporated on the CaF₂ substrates (fabrication of the films is described in the Supplementary Information, Section S2). It should be noted that the laser irradiation plane (x - z) was horizontal and the sample mounted vertical to avoid re-deposition of the laser-ablated material that could contaminate the sample.

The fabricated hole diameter was controlled via adjusting the energy of the focused laser pulse at the sample surface. To increase the range of attainable diameters, two different objective lenses with different numerical apertures have been used (NA1 = 0.25 and NA2 = 0.47). The results of the influence of the pulse energy on the hole diameter \varnothing for NA1 = 0.25 are displayed in Figure 3b, showing a predictive, increasing behavior with a bending at very high energies. This curve bending is a consequence of the Gaussian-like intensity distribution of the beam at the focal plane, further discussed in Section S3.1 from the Supplementary Material.^{33,34} This predictive and reproducible behavior allows one to calculate the output energy required for the fabrication of a specific hole diameter. An equivalent calibration curve of the hole diameter versus pulse energy was obtained also for NA = 0.47, as also detailed in Section S3.1 from the Supplementary Information. Importantly, the study of the influence of the energy on the diameter of the ablated spot was complemented with AFM topography measurements (see Supplementary Material Section S3.2), which revealed clean film ablation with sharp borders for both lenses, confirming that the pre-selected Au thickness (40 nm) was optimum for our experimental conditions.

The desired geometrical period Λ for a given metasurface was imprinted by high-speed scanning of the sample along the x-axis in a zigzag fashion, where the holes were fabricated via single pulse ablation (i.e., row by row). The periods in the x direction (Λ_x) were adjusted via modification of the scan velocity V_{scan} for a fixed F_{rep} , according to

$$\Lambda = \frac{V_{\text{scan}}}{F_{\text{rep}}} \quad (3)$$

whereas the periods in the y direction (Λ_y) were adjusted via discrete displacements of the y-motor after writing of each row.

Using this strategy, the maximum achievable processing speed is ultimately limited by the pulse repetition rate of the laser as well as by the sample scan velocity. All the devices reported in this work have been fabricated for a fixed repetition rate of $F_{\text{rep}} = 1 \text{ kHz}$, and different geometrical periods were achieved via varying V_{scan} . The purple line shown in Figure 3c corresponds to the prediction of the fabricated period Λ by eq 3. Such a linear relation was indeed experimentally verified over the entire range of periods studied ($\Lambda = 1.6\text{--}6.6 \mu\text{m}$), as confirmed by the red data points in Figure 3c. As also appreciated in the insets of Figure 3c, occasional stitching errors occur in some of the processed areas as a consequence of small delays of the motorized stage after writing each row (thus minor laser/stage synchronization mismatches). This affects the separation of holes written in different rows but not the separation of holes within the same row. As we will see in the Results section, this was found to have only minor effects on the optical response of our devices and could be minimized employing multiplexed beams for processing multiple holes in a single scan³⁵ or even eliminated by an improved synchronization between the translation stage and laser repetition rate.

3. RESULTS

A range of different EOT metasurfaces with areas of $2 \text{ mm} \times 2 \text{ mm}$ have been fabricated using the method described above, i.e., selecting the required NA, pulse energies, and scan velocity. The results presented below show their different

optical responses in terms of quality factor (Section 3.1), optical transmission peak (Section 3.2), and polarization-selective extraordinary transmission (Section 3.3).

3.1. EOT Devices with Different Quality Factors.

According to the simulations shown in Figure 2d,e, the Q -factor and amount of transmittance of the EOT device can be controlled via increasing the hole diameter \varnothing for a fixed period Λ and therefore via increasing the fill factor FF. To demonstrate this concept experimentally and highlight the flexibility of the laser processing approach, five different arrays with different hole diameters but identical periods have been fabricated. As detailed in Table S1 from the Supplementary Information (Section S4), all devices were processed using $V_{\text{scan}} = 6.6$ mm/s and $F_{\text{rep}} = 1$ kHz, yielding a period of $\Lambda = 6.6$ μm . Different pulse energies were used to adjust the hole diameters, and each device took 3 min to be fabricated. SEM images of the as-fabricated devices with nominal fill factors of FF = 0.48, FF = 0.53, FF = 0.55, FF = 0.56, and FF = 0.58 are displayed in Figure 4a. The

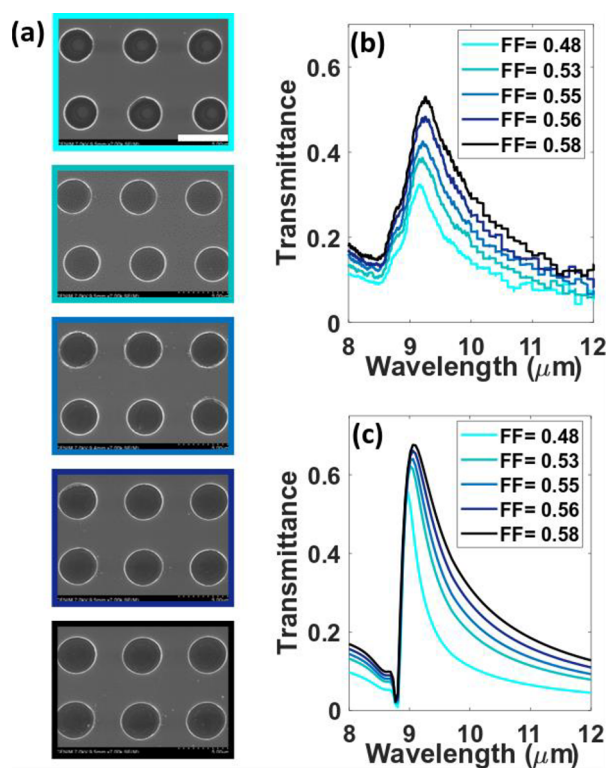


Figure 4. (a) SEM images of five different laser-fabricated EOT metasurface devices with different fill factors and identical geometrical period of $\Lambda = 6.6$ μm (scale bar is 5 μm). (b) FTIR measurements of the fabricated samples, revealing a progressive increase of the transmittance as the fill factor increases, in line with the predictions by numerical simulations shown in (c).

transmittance spectra of these devices were then measured using Fourier transform infrared spectroscopy (FTIR). The results are shown in Figure 4b, where an increase in transmittance of the EOT peak with a subsequent decrease in quality factor can be clearly observed as the fill factor increases. As the period of all devices was fixed, the transmission peak wavelength remains at a nearly stationary value ($\lambda_0 \sim 9.2$ μm). To compare our results with theoretical EOT performances, the as-fabricated dimensions of all the devices were introduced in COMSOL, and the transmittance

spectra were calculated yielding the results shown in Figure 4c. Indeed, a very good agreement with the experimental results was obtained, confirming the same overall shape of the transmission spectra, peak position, and spectral evolution of the measured devices (Figure 4b) when increasing the fill factor.

3.2. EOT Devices with On-Demand Transmission Peaks.

The capability of our fabrication method to generate extraordinary transmission at specific on-demand wavelength peaks was also explored. As shown in the previous sections (Figure 2b,c), this can be achieved via adjusting the period Λ between the holes. To this end, a new set of devices having different periods were fabricated and tested. As shown in Table S2 (Supplementary Information Section S4), the scanning speed was varied for a fixed repetition rate of 1 kHz, yielding as-fabricated periods of $\Lambda = 2.1$ μm ($V_{\text{scan}} = 2.0$ mm/s), $\Lambda = 4.1$ μm ($V_{\text{scan}} = 4.0$ mm/s), and $\Lambda = 6.6$ μm ($V_{\text{scan}} = 6.6$ mm/s), with total processing times of 19, 10, and 3 min, respectively. The pulse energy was adjusted accordingly to create spot sizes with an approximate fill factor FF = 0.5. For the lowest speed/smallest hole diameter, the high numerical aperture lens (NA = 0.47) was used (see energy vs hole diameter calibration in Figure S2b from the Supplementary Information). SEM images of the devices are shown in Figure 5a, and their transmittance spectra were measured employing FTIR. As shown in Figure 5b, the EOT peak shifts toward longer wavelengths as the period increases. Numerical

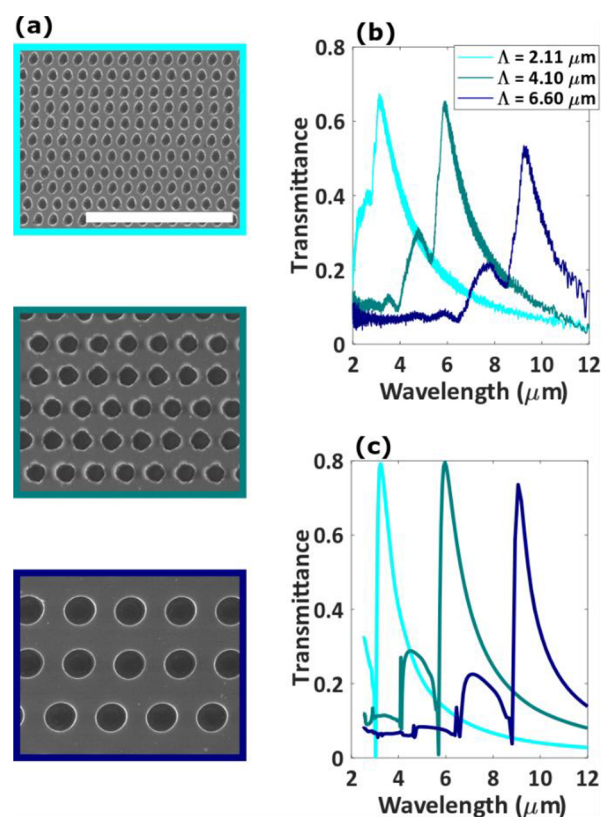


Figure 5. (a) SEM pictures of three laser-fabricated EOT metasurface devices with increasing geometrical periods (scale bar is 10 μm). (b) FTIR measurements of the fabricated samples, revealing a progressive increase of the transmission peak wavelength as the period increases. The results are in very good agreement with the numerical simulations shown in (c).

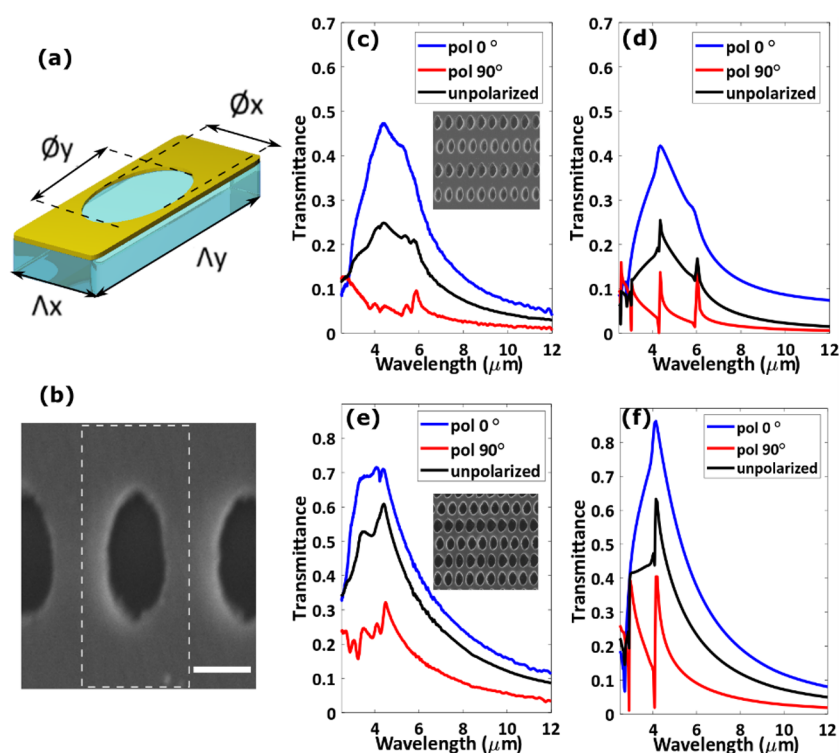


Figure 6. (a) Unit cell of EOT metasurfaces with polarization-selective optical response, where both period and diameters can be modified in two dimensions (x and y axes). (b) High magnification SEM image revealing fine details of the as-fabricated elliptical unit cells (scale bar is $1 \mu\text{m}$). (c) Measured and (d) simulated polarization selective transmittance spectra for device E1. The inset shows a SEM image of the device (field of view is $20 \mu\text{m} \times 18 \mu\text{m}$). (e) Measured and (f) simulated polarization-selective transmittance spectra for device E2. The inset shows an SEM image of the device (the same field of view as in (c)).

simulations of the optical response, using the period and hole diameters determined from the SEM images, are shown in Figure 5c. A good agreement with the experimental results is found also here. In particular, the peak positions and spectral widths predicted match well those of the measured devices. Moreover, the secondary transmission peak in the diffraction regime of each device, predicted by the calculations, is also present in our measurements. Finally, a general decrease of maximum transmittance ($\Delta T \sim 0.15$) is observed in the experiments with respect to simulations. This might be due to the imperfect hole shapes, small stitching errors, and roughness of the Au film itself (not taken into account in simulations). In particular, in Section S5 of the Supplementary Information, we explicitly show (via FEM simulations) how imperfections of the hole shapes have only minor effects on both the charge distribution of the metasurface when in resonance, as well as on its amount of transmittance.

3.3. EOT Devices with Polarization-Selective Response. Finally, the potential of our laser processing method to induce anisotropic optical responses for polarization-selective extraordinary transmission was also investigated. As depicted in Figure 6a, the square lattices were replaced by rectangular ones, giving rise to two different periods Λ_x and Λ_y . Moreover, the circular holes were replaced by elliptical ones, with different diameters in the x (Φ_x) and y (Φ_y) directions (Figure 6b). The required elliptical focal spots were achieved by inserting a slit aligned along the x -axis in the optical path of the laser processing line, as shown in Figure 3a. This way, the entrance pupil of the focusing aspheric lens (AL) is underfilled in the y -axis, leading to a reduced focusing and thus diameter increase along the y -axis. For a complete

description of the influence of the slit on the spot size, the modified beam divergence in the y -direction, leading to astigmatism, also needs to be taken into account.³⁶

As a proof of concept, two different arrays of elliptical holes in rectangular lattices (namely, E1 and E2) were fabricated. Table S3 from the Supplementary Information shows the laser parameters employed for their fabrication, as well as their as-fabricated dimensions. The period in the x -axis was fixed to $\Lambda_x = 2 \mu\text{m}$ in both devices. Φ_x was chosen to be larger and Λ_y smaller for E2 than for E1 to fabricate devices with different fill factors (and thus different amounts of transmittance). Each device took 8 min to be fabricated. The measured polarization-dependent transmission spectrum of device E1 is shown in Figure 6c, revealing a peak transmission for light polarized at 0° of $T \approx 0.5$ at a wavelength of $\lambda_0 \sim 4.2 \mu\text{m}$ and transmittance $T < 0.1$ for polarization at 90° . This strong polarization anisotropy was corroborated by the results of numerical simulations shown in Figure 6d, showing excellent agreement. It is worth noting that the predicted higher-order Wood anomalies possessing high Q -factors for 90° polarization are much weaker in the experimental results. This can be considered a beneficial side effect of the roughness of the films as well as of the small fluctuations in the hole diameter and lattice order achieved with the laser fabrication method. The presence of such small imperfections results, in this case, in an improved contrast ratio between the linear polarization states (i.e., $\Delta T = T(0^\circ)/T(90^\circ)$) when compared to the simulation.

The experimental transmittance spectrum for device E2 is displayed in Figure 6e, showing a similar behavior as device E1 but with a higher fill factor and narrower resonance. Both the

transmission peaks for polarization at 0° and 90° are higher than for E1, essentially due to a larger elliptical spot size (and smaller period in y) chosen, which is also confirmed by the calculations in Figure 6f. Also here, the predicted high-frequency resonances are efficiently attenuated.

4. CONCLUSIONS

We have demonstrated a versatile processing technique based on ultrafast DLW for the reliable fabrication of high-performance EOT metasurfaces. Contrary to lithographic-based fabrication methodologies, our technique enables the single-step realization of the EOT devices of several mm² in a few minutes, carried out in cleanroom-free environments without generating chemical residues. It was shown that the main performance characteristics of EOT devices in terms of transmission wavelength, amount of transmittance, and Q -factor can be controlled deliberately via tuning of the period Λ , the hole diameter \varnothing , and the hole ellipticity by means of adjustment of the sample scanning speed, laser pulse energy, and shape of the spot, respectively. These calibrations have then been successfully employed to fabricate various sets of devices with on-demand control of the transmission peak, Q -factor, and polarization sensitivity. FTIR measurements have revealed striking agreement between the as-fabricated and simulated devices, thus demonstrating the validity, flexibility, and versatility of our approach.

Based on the reported proof-of-concepts, it appears straightforward to fabricate cm² areas in the same times reported in this paper by means of exploiting the high-repetition rate of modern ultrafast laser systems and/or multiplexing techniques. The variety of fabricated shapes can be extended to more complex geometries using alternative beams (such as vortex beams for the fabrication of coaxial apertures)³⁷ based on the use of waveplates or spatial light modulators. Diameters down to 40 nm (i.e., far below the diffraction limit) have been reported in DLW processes,³⁸ and thus, both fabrication of deep-subwavelength structures and scalability of our approach toward shorter wavelengths (e.g., visible and near IR spectra) are also possible.

In conclusion, we believe that the proposed methodology could be applied not only to other metasurface geometries or materials but also for the rapid creation of large area molds for nanoimprint lithography, nanocasting, and stencils or masks for lift off processes.³⁹ Fabrication of more complex unit cells for alternative metasurface functionalities (such as multipixel meta-atoms containing different geometrical sizes for the fast processing of, e.g., beam steering devices^{6,40}) could be carried out via the use of multiple laser scans with different energies (thus different sizes of the ablation area).

■ ASSOCIATED CONTENT

SI Supporting Information

The Supporting Information is available free of charge at <https://pubs.acs.org/doi/10.1021/acsami.1c19935>.

The finite element model for EOT metasurfaces (S1). Fabrication of Au films on the CaF₂ substrates (S2). Dependence of the hole diameter with laser pulse energy (S3). Topography of the ablated region and idealness of the Au film thickness (S3.1). The laser processing parameters and as-fabricated dimensions of EOT metasurfaces (S4). Influence of the hole-shape imperfections on the optical response (S5) (PDF)

■ AUTHOR INFORMATION

Corresponding Authors

Carlota Ruiz de Galarreta – Laser Processing Group, Instituto de Óptica, IO-CSIC, Madrid 28006, Spain; College of Engineering, Mathematics and Physical Sciences, University of Exeter, Exeter EX4 4QF, UK; Email: cr408@io.cfmac.csic.es

Jan Siegel – Laser Processing Group, Instituto de Óptica, IO-CSIC, Madrid 28006, Spain; orcid.org/0000-0002-6159-7299; Email: j.siegel@csic.es

Authors

Noemi Casquero – Laser Processing Group, Instituto de Óptica, IO-CSIC, Madrid 28006, Spain; orcid.org/0000-0002-1194-6374

Euan Humphreys – College of Engineering, Mathematics and Physical Sciences, University of Exeter, Exeter EX4 4QF, UK

Jacopo Bertolotti – College of Engineering, Mathematics and Physical Sciences, University of Exeter, Exeter EX4 4QF, UK

Javier Solis – Laser Processing Group, Instituto de Óptica, IO-CSIC, Madrid 28006, Spain

C. David Wright – College of Engineering, Mathematics and Physical Sciences, University of Exeter, Exeter EX4 4QF, UK; orcid.org/0000-0003-4087-7467

Complete contact information is available at: <https://pubs.acs.org/10.1021/acsami.1c19935>

Author Contributions

[§]C.R.D. and N.C. contributed equally. The manuscript was written through contributions of all authors.

Funding

This work was financially supported by the Spanish Research Agency (MCIU/AEI/Spain) through project TEC2017-82464-R and PID2020-112770RB-C21, as well as by the National Research Council of Spain (CSIC) for the intramurales project 201850E057.

Notes

The authors declare no competing financial interest.

■ ACKNOWLEDGMENTS

The authors would like to thank Ms. Hannah Barnard and Prof. Geoffrey Nash (University of Exeter) for providing polarization-dependent FTIR measurements.

■ ABBREVIATIONS

AFM, atomic force microscopy
EOT, extraordinary optical transmission
FTIR, Fourier transform infrared spectroscopy
FF, fill factor
SEM, scanning electron microscopy
EBL, electron-beam lithography
ULP, ultrafast laser processing
DLW, direct laser writing

■ REFERENCES

- (1) Glybovski, S. B.; Tretyakov, S. A.; Belov, P. A.; Kivshar, Y. S.; Simovski, C. R. Metasurfaces: From Microwaves to Visible. *Phys. Rep.* **2016**, *634*, 1–72.
- (2) Yu, N.; Capasso, F. Flat Optics with Designer Metasurfaces. *Nat. Mater.* **2014**, *13*, 139–150.
- (3) Ruiz de Galarreta, C.; Carrillo, S. G.-C.; Au, Y.-Y.; Gemo, E.; Trimby, L.; Shields, J.; Humphreys, E.; Faneca, J.; Cai, L.; Baldycheva,

A.; Bertolotti, J.; Wright, C. D. Tunable Optical Metasurfaces Enabled by Chalcogenide Phase-Change Materials: From the Visible to the THz. *J. Opt.* **2020**, *22*, 114001.

(4) Ahmadiwand, A.; Semmlinger, M.; Dong, L.; Gerislioglu, B.; Nordlander, P.; Halas, N. J. Toroidal Dipole-Enhanced Third Harmonic Generation of Deep Ultraviolet Light Using Plasmonic Meta-Atoms. *Nano Lett.* **2019**, *19*, 605–611.

(5) Sharma, M.; Hendler, N.; Ellenbogen, T. Electrically Switchable Color Tags Based on Active Liquid-Crystal Plasmonic Metasurface Platform. *Adv. Opt. Mater.* **2020**, *8*, 1901182.

(6) de Galarreta, C. R.; Alexeev, A. M.; Au, Y. Y.; Lopez-Garcia, M.; Klemm, M.; Cryan, M.; Bertolotti, J.; Wright, C. D. Nonvolatile Reconfigurable Phase-Change Metadevices for Beam Steering in the Near Infrared. *Adv. Funct. Mater.* **2018**, 1704993.

(7) Yu, N.; Capasso, F. Optical Metasurfaces and Prospect of Their Applications Including Fiber Optics. *J. Light. Technol.* **2015**, *33*, 2344–2358.

(8) Solntsev, A. S.; Agarwal, G. S.; Kivshar, Y. S. Metasurfaces for Quantum Photonics. *Nat. Photonics* **2021**, *15*, 327–336.

(9) Alexeev, A.; Wright, D. C.; Alimagham, F.; Trimby, L.; Hutter, T. Metamaterials-Based IR Sensor with Internal Reference for Chemical Detection. *Imaging Appl. Opt. Congr. (2020), Pap. JW5C.6* **2020**, JW5C.6.

(10) Xie, L.; Gao, W.; Shu, J.; Ying, Y.; Kono, J. Extraordinary Sensitivity Enhancement by Metasurfaces in Terahertz Detection of Antibiotics. *Sci. Rep.* **2015**, 1–4.

(11) Gordon, R.; Sinton, D.; Kavanagh, K. L.; Brolo, A. G. A New Generation of Sensors Based on Extraordinary Optical Transmission. *Acc. Chem. Res.* **2008**, *41*, 1049.

(12) Sun, L. B.; Hu, X. L.; Zeng, B.; Wang, L. S.; Yang, S. M.; Tai, R. Z.; Fecht, H. J.; Zhang, D. X.; Jiang, J. Z. Effect of Relative Nanohole Position on Colour Purity of Ultrathin Plasmonic Subtractive Colour Filters. *Nanotechnology* **2015**, *26*, 305204.

(13) Rudé, M.; Mkhitarian, V.; Cetin, A. E.; Miller, T. A.; Carrilero, A.; Wall, S.; de Abajo, F. J. G.; Altug, H.; Pruneri, V. Ultrafast and Broadband Tuning of Resonant Optical Nanostructures Using Phase-Change Materials. *Adv. Opt. Mater.* **2016**, *4*, 1060–1066.

(14) Barnes, W. L.; Murray, W. A.; Dintinger, J.; Devaux, E.; Ebbesen, T. W. Surface Plasmon Polaritons and Their Role in the Enhanced Transmission of Light through Periodic Arrays of Subwavelength Holes in a Metal Film. *Phys. Rev. Lett.* **2004**, *92*, 107401.

(15) De Abajo, F. J. G. Colloquium: Light Scattering by Particle and Hole Arrays. *Rev. Mod. Phys.* **2007**, *79*, 1267–1290.

(16) Su, V. C.; Chu, C. H.; Sun, G.; Tsai, D. P. Advances in Optical Metasurfaces: Fabrication and Applications [Invited]. *Opt. Express* **2018**, *26*, 13148–13182.

(17) Dudley, R. A.; Fiddy, M. A.; Society of Photo-optical Instrumentation Engineers. ISBN 9781510602151. *Engineered Materials and Metamaterials: Design and Fabrication*; 2017th ed.; SPIE Press Book.

(18) Boltasseva, A.; Shalae, V. M. Fabrication of Optical Negative-Index Metamaterials: Recent Advances and Outlook. *Metamaterials* **2008**, *2*, 1–17.

(19) Walia, S.; Shah, C. M.; Gutruf, P.; Nili, H.; Chowdhury, D. R.; Withayachumnankul, W.; Bhaskaran, M.; Sriram, S. Flexible Metasurfaces and Metamaterials: A Review of Materials and Fabrication Processes at Micro- and Nano-Scales. *Appl. Phys. Rev.* **2015**, *2*, No. 011303.

(20) Stratakis, E.; Bonse, J.; Heitz, J.; Siegel, J.; Tsiibidis, G. D.; Skoulas, E.; Papadopoulos, A.; Mimidis, A.; Joel, A. C.; Comanns, P.; Krüger, J.; Florian, C.; Fuentes-Edfuf, Y.; Solis, J.; Baumgartner, W. Laser Engineering of Biomimetic Surfaces. *Mater. Sci. Eng. R* **2020**, *141*, 100562.

(21) Stoian, R.; Colombier, J.-P. Advances in Ultrafast Laser Structuring of Materials at the Nanoscale. *NANO* **2020**, *9*, 4665–4688.

(22) Kazansky, P. G.; Lei, Y.; Wang, L.; Yu, Y.; Wang, H.; Corres, A.; Spivack, N.; Sarao, B. Eternal 5d Data Storage by Ultrafast Laser

Writing in Glass. *Accel. Sp. Commer. Explor. New Discov. Conf. ASCEND 2020* **2020**, 97360U.

(23) Osellame, R.; Cerullo, G.; Ramponi, R. *Femtosecond Laser Micromachining: Photonic and Microfluidic Devices in Transparent Materials*; Springer Science & Business Media: 2012, 123, DOI: 10.1007/978-3-642-23366-1.

(24) Florian, C.; Skoulas, E.; Puerto, D.; Mimidis, A.; Stratakis, E.; Solis, J.; Siegel, J. Controlling the Wettability of Steel Surfaces Processed with Femtosecond Laser Pulses. *ACS Appl. Mater. Interfaces* **2018**, *10*, 36564–36571.

(25) Yong, J.; Chen, F.; Yang, Q.; Hou, X. Femtosecond Laser Controlled Wettability of Solid Surfaces. *Soft Matter* **2015**, *11*, 8897–8906.

(26) Berzinš, J.; Indrišūnas, S.; van Erve, K.; Nagarajan, A.; Fasold, S.; Steinert, M.; Gerini, G.; Gečys, P.; Pertsch, T.; Bäumer, S. M. B.; Setzpfandt, F. Direct and High-Throughput Fabrication of Mie-Resonant Metasurfaces via Single-Pulse Laser Interference. *ACS Nano* **2020**, *14*, 6138–6149.

(27) Zywiets, U.; Evlyukhin, A. B.; Reinhardt, C.; Chichkov, B. N. Laser Printing of Silicon Nanoparticles with Resonant Optical Electric and Magnetic Responses. *Nat. Commun.* **2014**, *5*, 3402.

(28) Stankevičius, E.; Vilkevičius, K.; Gedvilas, M.; Bužavaitė-Vertelienė, E.; Selskis, A.; Balevičius, Z. Direct Laser Writing for the Formation of Large-Scale Gold Microbumps Arrays Generating Hybrid Lattice Plasmon Polaritons in Vis–NIR Range (Advanced Optical Materials 12/2021). *Adv. Opt. Mater.* **2021**, *9*, 2170044.

(29) Yoo, J.-H.; Nguyen, H. T.; Ray, N. J.; Johnson, M. A.; Steele, W. A.; Chesser, J. M.; Baxamusa, S. H.; Elhadj, S.; McKeown, J. T.; Matthews, M. J.; Feigenbaum, E. Scalable Light-Printing of Substrate-Engraved Free-Form Metasurfaces. *ACS Appl. Mater. Interfaces* **2019**, 22684.

(30) Destouches, N.; Sharma, N.; Vangheluwe, M.; Dalloz, N.; Vocanson, F.; Bugnet, M.; Hébert, M.; Siegel, J. Laser-Empowered Random Metasurfaces for White Light Printed Image Multiplexing. *Adv. Funct. Mater.* **2021**, *31*, 2010430.

(31) Li, H. H. Refractive Index of Alkaline Earth Halides and Its Wavelength and Temperature Derivatives. *J. Phys. Chem. Ref. Data* **1980**, *9*, 161.

(32) Macias-Montero, M.; Dias, A.; Sotillo, B.; Moreno-Zarate, P.; Ariza, R.; Fernandez, P.; Solis, J. Waveguide Tapers Fabrication by Femtosecond Laser Induced Element Redistribution in Glass. *J. Light. Technol.* **2020**, *38*, 6578–6583.

(33) Liu, J. M. Simple Technique for Measurements of Pulsed Gaussian-Beam Spot Sizes. *Opt. Lett.* **1982**, *7*, 196–198.

(34) Garcia-Lechuga, M.; Grojo, D. Simple and Robust Method for Determination of Laser Fluence Thresholds for Material Modifications: An Extension of Liuns Approach to Imperfect Beams. *Open Res. Eur.* **2021**, *1*, 7.

(35) Kuchmizhak, A. A.; Porfirev, A. P.; Pavlov, D.; Lapine, M.; Vitrik, O. B.; Danilov, P. A.; Gurbatov, S.; Kulinich, S. A.; Kudryashov, S. I.; Khonina, S. N. 10-Million-Elements-per-Second Printing of Infrared-Resonant Plasmonic Arrays by Multiplexed Laser Pulses. *Opt. Lett.* **2019**, *44*, 283–286.

(36) De la Cruz, A. R.; Ferrer, A.; del Hoyo, J.; Siegel, J.; Solis, J. Modeling of Astigmatic-Elliptical Beam Shaping during Fs-Laser Waveguide Writing Including Beam Truncation and Diffraction Effects. *Appl. Phys. A: Mater. Sci. Process.* **2011**, *104*, 687–693.

(37) Pavlov, D.; Porfirev, A.; Khonina, S.; Pan, L.; Kudryashov, S. I.; Kuchmizhak, A. A. Coaxial Hole Array Fabricated by Ultrafast Femtosecond-Laser Processing with Spatially Multiplexed Vortex Beams for Surface Enhanced Infrared Absorption. *Appl. Surf. Sci.* **2021**, *541*, 148602.

(38) Joglekar, A. P.; Liu, H. H.; Meyhöfer, E.; Mourou, G.; Hunt, A. J. Optics at Critical Intensity: Applications to Nanomorphing. *Proc. Natl. Acad. Sci.* **2004**, *101*, 5856–5861.

(39) Kim, K.; Yoon, G.; Baek, S.; Rho, J.; Lee, H. Facile Nanocasting of Dielectric Metasurfaces with Sub-100 Nm Resolution. *ACS Appl. Mater. Interfaces* **2019**, *11*, 26109–26115.

(40) Zou, L.; Withayachumnankul, W.; Shah, C. M.; Mitchell, A.; Bhaskaran, M.; Sriram, S.; Fumeaux, C. Dielectric Resonator Nanoantennas at Visible Frequencies. *Opt. Express* **2013**, *21*, 1344.

Recommended by ACS

High-Efficiency Plasmonic Metalens for Dual-Polarization Imaging with a Single Set of 3D Variable Nanostructures

Ti Sun, Chinhua Wang, *et al.*

AUGUST 09, 2022
ACS PHOTONICS

READ 

Structure and Optical Property Prediction of 2D Plasmonic Photonic Crystals Fabricated by Shadow Sphere Lithography

Yanfeng Wang, Yiping Zhao, *et al.*

DECEMBER 06, 2022
ACS APPLIED NANO MATERIALS

READ 

Fourier-Engineered Plasmonic Lattice Resonances

Theng-Loo Lim, Robert W. Boyd, *et al.*

MARCH 31, 2022
ACS NANO

READ 

Remote Dual-Cavity Enhanced Second Harmonic Generation in a Hybrid Plasmonic Waveguide

Junjun Shi, Hongxing Xu, *et al.*

JANUARY 13, 2022
NANO LETTERS

READ 

Get More Suggestions >